Sensitivity-based characterization of the bias errors in frequency based substructuring

Gregor Čepon[a,*], Domen Ocepek[a], Jure Korbar[a], Tomaž Bregar[b], Miha Boltežar[a]

[a]*Faculty of Mechanical Engineering, University of Ljubljana, Aškerčeva 6, 1000 Ljubljana, Slovenia*
[b]*Gorenje d.o.o., Partizanska 12, 3503 Velenje, Slovenia*

Cite as:
Gregor Čepon, Domen Ocepek, Jure Korbar, Tomaž Bregar, Miha Boltežar, Sensitivity-based characterization of the bias errors in frequency based substructuring, Mechanical Systems and Signal Processing, 2022, https://doi.org/10.1016/j.ymssp.2021.108800

Abstract

A reliable experimental application of frequency based substructuring requires very accurate acquisition of frequency response functions (FRFs). Even a relatively small error introduced during the measurement can result in erroneous substructuring results. The measurement errors can be either random or systematic, with the latter often referred to as bias. Impact excitation is popular in dynamic substructuring due to the rapid FRF calculation for each separate location. However, deviations in the location of the excitation affect the FRFs across the whole frequency range. This paper proposes a novel methodology to characterize the bias errors in frequency based substructuring using the small deviations in impact excitation from typical experimental measurements. The small deviations are utilized to reconstruct a range of FRFs, which are directly used in the global sensitivity analysis. The sensitivity analysis is utilized to characterize how each impact location affects an arbitrary quality indicator, such as reciprocity or passivity. Therefore, the effect of the bias can be evaluated directly from a single series of measurements, without the need for a numerical

*Corresponding author
Email address: `gregor.cepon@fs.uni-lj.si` (Gregor Čepon)

model. The proposed approach is first shown on a synthetic numerical example, where the advantages and limitations are outlined. Finally, an application involving experimental frequency based substructuring on a beam-like structure is depicted.

Keywords: frequency based substructuring, virtual point transformation, bias error, global sensitivity analysis

1 Introduction

Dividing large and complex systems into several subsystems is a common practice in the field of structural dynamics. Structural dynamic analyses can be carried out more efficiently if the complex systems are divided into smaller subsystems, analysed separately, and later coupled using dynamic substructuring (DS) methods. Depending on the substructures' response models, which can be either experimental or numerical, an arbitrary domain can be used to implement the DS methods [1]. However, the majority of the research content relates to the frequency and the modal domain. Within the modal domain, the component-mode synthesis (CMS) formulations are widely used in numerical applications [2]. On the other hand, frequency based substructuring (FBS) methods [3] are usually related to the experimental approach, as it is possible to define the exact dynamic properties directly based on the measured frequency response functions (FRFs) [4].

Although FBS methods are well established, the challenge to provide accurate and reliable dynamic properties for the individual subsystem remains. The application to complex, real-life engineering structures is often hindered by the experimental errors [5–7]. Accurate measurement of the FRFs is essential, as the errors in the substructure's FRFs are propagated and amplified in the assembled FRFs [5]. In general, the measurement errors can be classified according to their nature into two categories: random errors and systematic errors (also called bias).

An error of a random nature is referred to as the measurement uncertainty.

Several sources of random errors are accounted for while performing dynamic measurements: sensor noise, rounding-off errors in A/D conversion, environmental noise, and other uncontrollable factors. The propagation of uncertainty in FBS was initially investigated by Voormeeren et al. [8] under the assumption of an uncorrelated uncertainty. Meggit and Moorhouse [9] proposed a generalized framework for uncertainty propagation in FRF-based DS. Trainotti et al. [10] provided a practical and reliable methodology for the quantification of the random measurement uncertainty in FBS applications. The proposed framework presents a covariance-based approach for quantifying the uncertainty in measured FRFs and their propagation through interface modelling and substructure-coupling approaches. In [10], it was concluded that very precise measurements (small random errors) lead to narrow confidence bounds; however, the measured FRFs can still contain very distorted information due to the bias errors.

An error defined as systematic is consistent and repeatable in nature. The effect of bias can be observed as a systematic shift in the measurement results; therefore, it does not affect the reliability, but rather directly the accuracy of the outcome. Discarding rotational degrees of freedom and non-collocated DoFs at the interface can be considered as the most prominent systematic error [11]. Both of the above-mentioned difficulties can be resolved using virtual point transformation (VPT) [12, 13]. Based on the interface deformation modes (IDMs) a full-DoF virtual point's (VP's) admittance matrix is reconstructed with perfectly collocated DoFs for each substructure. Since IDMs are defined using the relative impact and response locations with regard to the VP, any error in the location/orientation offset can lead to an inconsistent VPT. In general, an erroneous position/orientation of the excitation and response measurement are common examples of measurement bias that affect the experimental substructuring. Careful design of the experiment and system modelling helps to minimize the influence of those errors. However, if the structure is excited with the impulse hammer by hand, it would likely be difficult to achieve sufficient repeatability in the impact location. An experimental study of the errors introduced by a misalignment of the excitation was initially investigated by De Klerk and Visser [6] and later by De Klerk [14] for the driving-point FRFs. It was demonstrated that the offset in the impact locations and the orientations influence the amplitude of the eigenfrequencies, as well as the frequency of the anti-resonances. A further investigation into bias errors within the FBS led to the development of a method for the automated correction of the sensor orientation in the scope of the VPT [15]. It is shown that this optimization can largely remove the incorrect position estimates in the input and output locations, but the method has only been tested on numerical case studies.

The objective of this paper is to develop a sensitivity-based approach to characterize the bias errors in experimental DS. Sensitivity analysis is introduced to characterize the influence of the impact location offset with respect to the consistency of the VPT, which is applied to successfully couple both substructures, weaken the interface problem and to some extent filter the measurement errors due to a reduction of the displacements and forces. However, as the transformation is based on the relative locations and orientations of the impacts and responses with respect to the VP, bias errors affect the VP admittance. To identify the influence of the bias error in the VPT and the coupling process in general, the idea is not to average the measurements at the location of the individual force input, but to use them as a subset for the sensitivity analysis. However, in order to be able to perform the global sensitivity analysis exclusively with the experimental response model, numerous biased FRFs should be measured at each impact location. This is practically impossible. Therefore, a linear relationship between the biased FRFs and the location offset was adopted [6, 14] in order to be able to construct a sizable FRF set following Saltelli sampling scheme [16]. FRF set is intended to be used in Sobol's sensitivity analysis [17, 18] in order to simultaneously evaluate the relative contribution of each individual biased force input as well as their interactions on the variance of the reconstructed VP's reciprocity. The proposed method enables the identification of the impact locations where the bias error would have the greatest influence on the consistency of the VPT. To present the efficiency of the proposed approach, both a numerical and experimental case study are presented. It is demonstrated that removing impacts with high sensitivity indices from the coupling process improves the efficiency and accuracy of the coupling results.

The paper is organized as follows. The following section briefly summarizes the theory of the Lagrange multiplier frequency based substructuring (LM FBS) method and the VPT. Next, the algorithm for characterization of the bias error is presented in Section 3. The algorithm is presented using numerical verification, for the sake of better clarity. In Section 4 an experimental validation is presented and finally the conclusions are drawn in Section 5.

2 Frequency based substructuring

In order to couple substructures based on their frequency response models, the LM FBS method [3] is adopted here.

2.1 LM FBS method

The LM FBS method makes it possible to determine the assembled system admittance $\mathbf{Y}^{\mathrm{AB}}$ in which the FRFs of the individual subsystems are considered. The equation of motion for the uncoupled substructures, depicted in Fig. 1a, in the frequency domain is:

$$\boldsymbol{u}(\omega) = \mathbf{Y}^{\mathrm{A|B}}(\omega)\big(\boldsymbol{f}(\omega) + \boldsymbol{g}(\omega)\big). \tag{1}$$

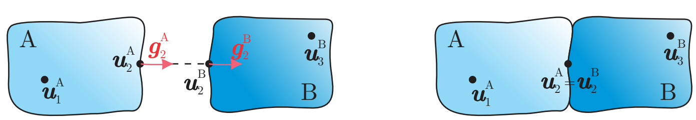

(a)

(b)

Figure 1: Schematic overview of the substructuring problem; a) Uncoupled substructures A and B, b) Coupled assembly AB.

The vector $\boldsymbol{u}(\omega)$ represents the responses to the external force vector $\boldsymbol{f}(\omega)$, applied to the coupled configuration, and $\boldsymbol{g}(\omega)$ is the vector of interface forces between the substructures in the coupled state. Admittance matrices of each substructure are assembled into a block-diagonal matrix $\mathbf{Y}^{\mathrm{A|B}}$:[1]

$$\boldsymbol{u} = \begin{bmatrix} \boldsymbol{u}_1^{\mathrm{A}} \\ \boldsymbol{u}_2^{\mathrm{A}} \\ \boldsymbol{u}_2^{\mathrm{B}} \\ \boldsymbol{u}_3^{\mathrm{B}} \end{bmatrix}, \quad \mathbf{Y}^{\mathrm{A|B}} = \begin{bmatrix} \mathbf{Y}_{11}^{\mathrm{A}} & \mathbf{Y}_{12}^{\mathrm{A}} & \mathbf{0} & \mathbf{0} \\ \mathbf{Y}_{21}^{\mathrm{A}} & \mathbf{Y}_{22}^{\mathrm{A}} & \mathbf{0} & \mathbf{0} \\ \mathbf{0} & \mathbf{0} & \mathbf{Y}_{22}^{\mathrm{B}} & \mathbf{Y}_{23}^{\mathrm{B}} \\ \mathbf{0} & \mathbf{0} & \mathbf{Y}_{32}^{\mathrm{B}} & \mathbf{Y}_{33}^{\mathrm{B}} \end{bmatrix}, \quad \boldsymbol{f} = \begin{bmatrix} \boldsymbol{f}_1^{\mathrm{A}} \\ \boldsymbol{f}_2^{\mathrm{A}} \\ \boldsymbol{f}_2^{\mathrm{B}} \\ \boldsymbol{f}_3^{\mathrm{B}} \end{bmatrix}, \quad \boldsymbol{g} = \begin{bmatrix} \mathbf{0} \\ \boldsymbol{g}_2^{\mathrm{A}} \\ \boldsymbol{g}_2^{\mathrm{B}} \\ \mathbf{0} \end{bmatrix}. \tag{2}$$

The compatibility conditions between the substructures are written through the Boolean matrix $\mathbf{B}$ (Eq. (3)), which ensures that the substructures have the same displacements at the interface in the coupled state (Fig. 1b). The equilibrium conditions (Eq. (4)) are introduced by choosing the interface forces using a set of unknown Lagrange multiplier vectors $\boldsymbol{\lambda}$.

$$\mathbf{B}\,\boldsymbol{u} = \mathbf{0} \tag{3}$$

$$\boldsymbol{g} = -\mathbf{B}^{\mathrm{T}}\boldsymbol{\lambda} \tag{4}$$

Solving the set of Eqs. (2 - 4) and eliminating the Lagrange multiplier vector yields the response of the coupled structure:

$$\boldsymbol{u} = \mathbf{Y}^{\mathrm{AB}}\,\boldsymbol{f} = \left[\mathbf{Y}^{\mathrm{A|B}} - \mathbf{Y}^{\mathrm{A|B}}\,\mathbf{B}^{\mathrm{T}}\,\left(\mathbf{B}\,\mathbf{Y}^{\mathrm{A|B}}\,\mathbf{B}^{\mathrm{T}}\right)^{-1}\,\mathbf{B}\,\mathbf{Y}^{\mathrm{A|B}}\right]\boldsymbol{f}. \tag{5}$$

The dynamic properties of the assembled system are governed by the coupled admittance matrix $\mathbf{Y}^{\mathrm{AB}}$. The LM FBS method requires the full-DoF response models of individual substructures with DoFs at the interface collocating for all substructures. However, the DoFs measured on both sides of the interface usually do not match when it comes to the experimental testing of the substructures with complex geometries. Even if the collocation could be achieved, the lack of RDoFs would impose a problem. Both aforementioned problems can be resolved using the VPT, allowing to locate virtual points at the interface identically for the substructures to couple and thus solve collocation issues.

[1] An explicit dependence on the frequency is omitted to improve the readability of the notation, as will be the case for the remainder of the paper.

2.2 Virtual point transformation

A virtual point is chosen near the physical interface of the substructures at which the admittance matrix is obtained using a geometrical transformation. Multiple responses and excitations are measured close to this point ($\mathbf{Y}_{\mathrm{uf}} \in \mathbb{C}^{n_{\mathrm{u}} \times n_{\mathrm{f}}}$) and then projected onto the interface deformation modes (IDMs). If only the rigid-body IDMs are included in the transformation then we have $m = 6$ DoFs for each virtual point (three translational and three rotational DoFs). If the interface exhibits more complex dynamic behaviour, flexible IDMs can also be added [13]. The transformation is achieved using the following equation:

$$\mathbf{Y}_{\mathrm{qm}} = \mathbf{T}_{\mathrm{u}} \mathbf{Y}_{\mathrm{uf}} \mathbf{T}_{\mathrm{f}}^{\mathrm{T}}, \tag{6}$$

where $\mathbf{T}_{\mathrm{u}}$ is the displacement transformation matrix and $\mathbf{T}_{\mathrm{f}}$ is the force transformation matrix. $\mathbf{Y}_{\mathrm{qm}} \in \mathbb{C}^{m \times m}$ is the VP admittance matrix with a perfectly collocated translation/rotation and force/moment DoFs.

The following relation can be written between the m VP responses $\boldsymbol{q} = [q_X, q_Y, q_Z, q_{\theta_X}, q_{\theta_Y}, q_{\theta_Z}]^{\mathrm{T}}$ and the n_{u} sensor displacements $\boldsymbol{u}$ ($m < n_{\mathrm{u}}$):

$$\boldsymbol{u} = \mathbf{R}_{\mathrm{u}} \boldsymbol{q}. \tag{7}$$

The columns of a $\mathbf{R}_{\mathrm{u}} \in \mathbb{R}^{n_{\mathrm{u}} \times m}$ consist of IDMs constructed from the relative sensor locations and orientations with respect to the VP (Fig. 2). For more information about the assembly of the $\mathbf{R}_{\mathrm{u}}$ the reader is referred to [12]. Solving Eq. (7) for $\boldsymbol{q}$ in a least-square sense yields the displacements of the VP[2]:

$$\boldsymbol{q} = \left(\mathbf{R}_{\mathrm{u}}^{\mathrm{T}} \mathbf{R}_{\mathrm{u}}\right)^{-1} \mathbf{R}_{\mathrm{u}}^{\mathrm{T}} \boldsymbol{u} = \mathbf{T}_{\mathrm{u}} \boldsymbol{u} \quad \Rightarrow \quad \mathbf{T}_{\mathrm{u}} = \left(\mathbf{R}_{\mathrm{u}}^{\mathrm{T}} \mathbf{R}_{\mathrm{u}}\right)^{-1} \mathbf{R}_{\mathrm{u}}^{\mathrm{T}}. \tag{8}$$

Similarly, the loads at the virtual point $\boldsymbol{m} = [m_X, m_Y, m_Z, m_{\theta_X}, m_{\theta_Y}, m_{\theta_Z}]^{\mathrm{T}}$ are obtained for a measured vector of forces $\boldsymbol{f}$. The contribution from all the input forces can be combined and expressed as follows:

$$\mathbf{m} = \mathbf{R}_{\mathrm{f}}^{\mathrm{T}} \mathbf{f}, \tag{9}$$

[2]To gain more flexibility over the transformation, a frequency-dependent symmetrical weighting matrix $\mathbf{W}$ can be added to the derivation of $\boldsymbol{q}$, see [1].

where $\mathbf{R}_{\mathrm{f}}^{\mathrm{T}} \in \mathbb{R}^{m \times n_{\mathrm{f}}}$ is the matrix containing the positions and orientations

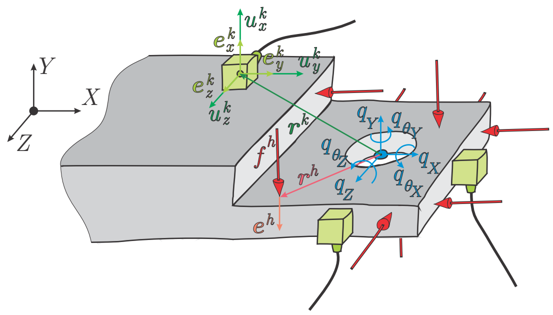

Figure 2: Interface connection example using virtual point[3].

for all the impact locations with respect to the VP. A more detailed description of $\mathbf{R}_{\mathrm{f}}$ is given in [12]. Solving Eq. (9) for optimal $\boldsymbol{f}$ we obtain the following expression:

$$\boldsymbol{f} = \mathbf{R}_{\mathrm{f}}\Big(\mathbf{R}_{\mathrm{f}}^{\mathrm{T}}\mathbf{R}_{\mathrm{f}}\Big)^{-1}\boldsymbol{m} = \mathbf{T}_{\mathrm{f}}^{\mathrm{T}}\boldsymbol{m} \quad \Rightarrow \quad \mathbf{T}_{\mathrm{f}}^{\mathrm{T}} = \mathbf{R}_{\mathrm{f}}\Big(\mathbf{R}_{\mathrm{f}}^{\mathrm{T}}\mathbf{R}_{\mathrm{f}}\Big)^{-1}. \tag{10}$$

As the VP DoFs are perfectly collocated, the FRF matrix should be reciprocal. A reciprocity evaluation can therefore be used to assess the quality of the transformation. A coherence criterion is applied to compare the individual VP FRFs [12]:

$$\chi_{ij} = \mathrm{coh}\big(Y_{ij},\, Y_{ji}\big) = \frac{(Y_{ij} + Y_{ji})(Y_{ij}^* + Y_{ji}^*)}{2\,(Y_{ij}\,Y_{ij}^* + Y_{ji}\,Y_{ji}^*)}, \quad Y_{ij},\, Y_{ji} \in \mathbf{Y}_{\mathrm{qm}}, \tag{11}$$

where $*$ denotes a complex conjugate. The criterion is bounded between 0 and 1, where the values closer to 1 indicate a strong correlation between two reciprocal VP FRFs. However, for the diagonal elements the coherence criterion equals 1 by definition ($\chi_{ii} = 1$). For the diagonal FRFs, the passivity can be evaluated since the driving-point FRFs should always be minimum-phase

[3] The position vector from the VP to the center of the triaxial accelerometer is denoted by $\boldsymbol{r}^k$. The unit vector for each sensor axis is $\boldsymbol{e}_i^k$ and the response in each axis is denoted by u_i^k ($i \in (x,\, y,\, z)$). The position vector from VP to the force impact is $\boldsymbol{r}^h$, the impact direction is $\boldsymbol{e}^h$ and the impact magnitude is f^h.

functions. Therefore, the phase of the driving-point FRFs should always be bounded by $\angle Y_{ii} \in [0°, 180°]$ for accelerance FRFs.

2.3 Notes on the bias-affected VPT

Appropriate positions for the sensors and the impact locations are necessary to obtain a consistent virtual point transformation. The sensors and impact locations should be close to the VP to avoid the local deformation around it. However, with a decreased distance the uncertainties associated with the position and orientation are increased. The response and excitation positions are usually evaluated after the VPT using the measurement-quality indicators [1]. These indications compare the original with the filtered measurements (measurements transformed to the VP and then projected back to the initial location) using the coherence criterion. However, it is difficult to robustly characterize the bias of the individual impact/channel with regards to the quality of the VPT .

Bias errors are manifested in the inconsistent matrices $\mathbf{R}_{\mathrm{u}}$ and $\mathbf{R}_{\mathrm{f}}$, assembled using known sensor and impact locations and orientations. From the practical point of view, bias errors emerge mainly due to the poor repeatability of the structure's excitation by hand using a modal hammer. Regarding the sensor placement and position, bias errors can be greatly reduced with careful fitting of the sensor to the structure and a precise determination of its location. Therefore, it is not considered critical to the quality of the VPT.

3 Identification of biased force inputs in the VPT

The following section presents the proposed method for the characterization of bias errors in experimental dynamic substructuring. In order to clearly demonstrate the idea, the method is formulated on a synthetic, numerical case study. The application simulates a coupling process between two substructures with one VP. In Fig. 3 substructures A and B are shown in the uncoupled and coupled configurations using an open-source Python package *pyFBS* [19]. A bolted connection is proposed to assemble the substructures. In order to perform the coupling, the interface is reduced to a single virtual point, as shown in Fig. 3.

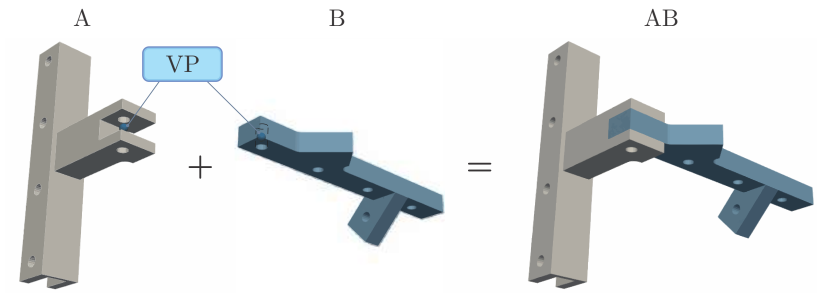

Figure 3: Coupling process of the substructures A and B.

Step 1: Acquisition of biased FRFs

The first step of the proposed methodology consists of multiple FRF measurements for each impact location, as would usually be the case, to average and use them in a dynamic coupling process (schematically presented in Fig. 4). For this numerical example, the dynamic responses for the substructures A and

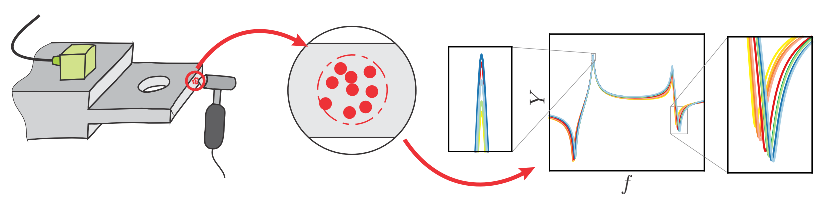

Figure 4: Step 1: Measurement of the multiple FRFs at each impact location.

B are obtained from the finite-element analysis, proposing free-free boundary conditions. The material properties of the analysed structures are presented in Table 1. For each substructure, the FRFs were synthesised. No bias errors were assumed for the structure B, where the FRFs were synthesised at nine response and nine impact locations around the VP. Fifteen different impact locations were simulated in the vicinity of the interface at the structure A, which are schematically presented in Fig. 5. Uncertainties with respect to the location of

Table 1: Beam-like structure's material properties.

Parameter	Unit	Value
ρ	kg/m^3	2750
E	GPa	70

the impact were simulated with a force location offset. We assume here that all the impact locations are placed close to the desired excitation position, bounded by and distributed randomly within a circle. No location offset was set for the response location.

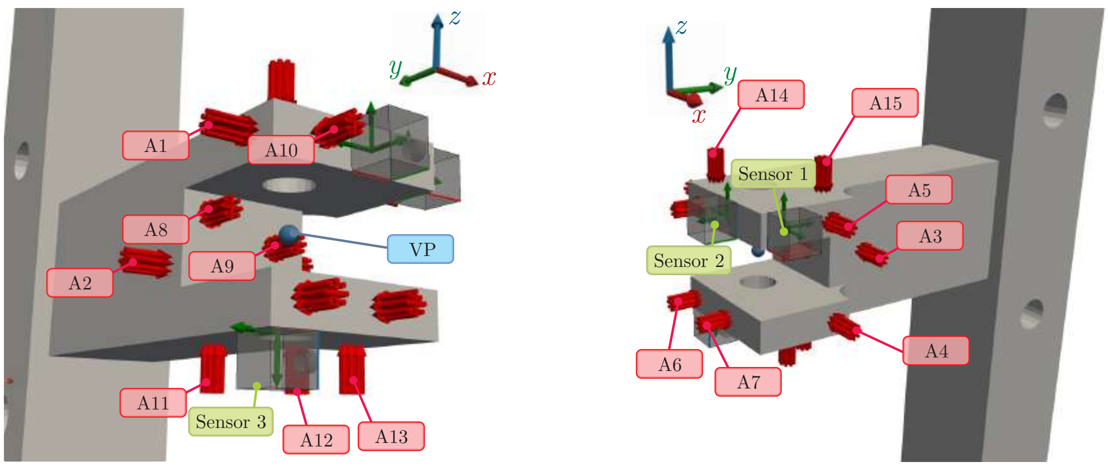

(a)

(b)

Figure 5: Presentation of the virtual point for substructure A together with the channel and impact locations; a) Left view, b) Right view.

An example of impact bias-affected FRFs for one impact and one response location is shown in Fig. 6. Fig. 7 shows the real and imaginary parts versus the location offset in the x and y directions for a selected frequency value. The results show that for a small unidirectional offset in excitation location, changes in real and imaginary part are linear.

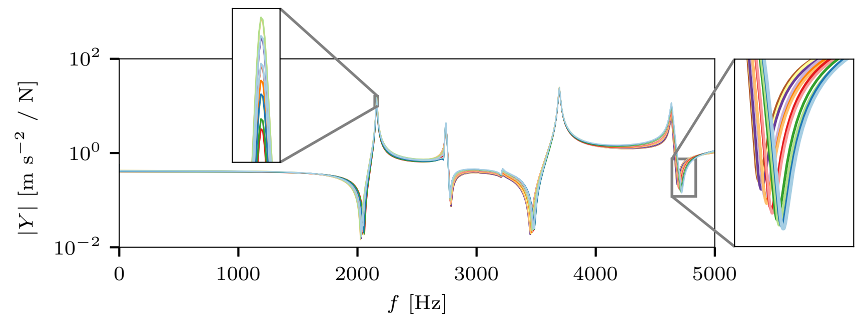

Figure 6: Impact bias-affected FRFs for impact location A2 and sensor location 1, x-direction.

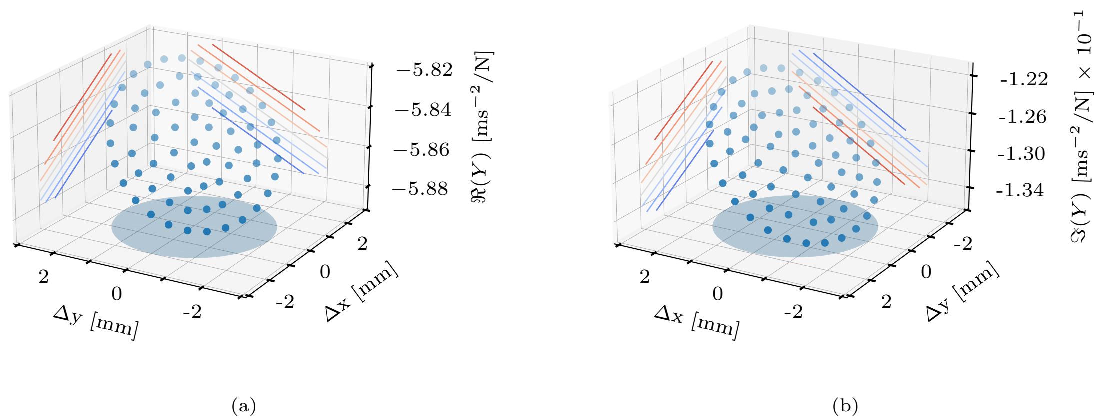

Figure 7: Linear relation of FRF amplitude with respect to bias for impact location A2 and sensor location 1, x-direction, at a frequency of 2000 Hz; a) Real part, b) Imaginary part.

Step 2: Evaluation of biased FRFs

By plotting the bias-affected FRFs to the complex plane at each frequency, a bias error is reflected in the FRFs distributed within an ellipse in Fig. 8. For equidistant bias errors the impacts located on the ellipse's major axis cause greatest differences in FRF's real in imaginary part. Hence the major axis is orientated in a direction where the FRFs are most sensitive to a unidirectional bias.

The equation of the ellipse's major axis can be determined using an approx-

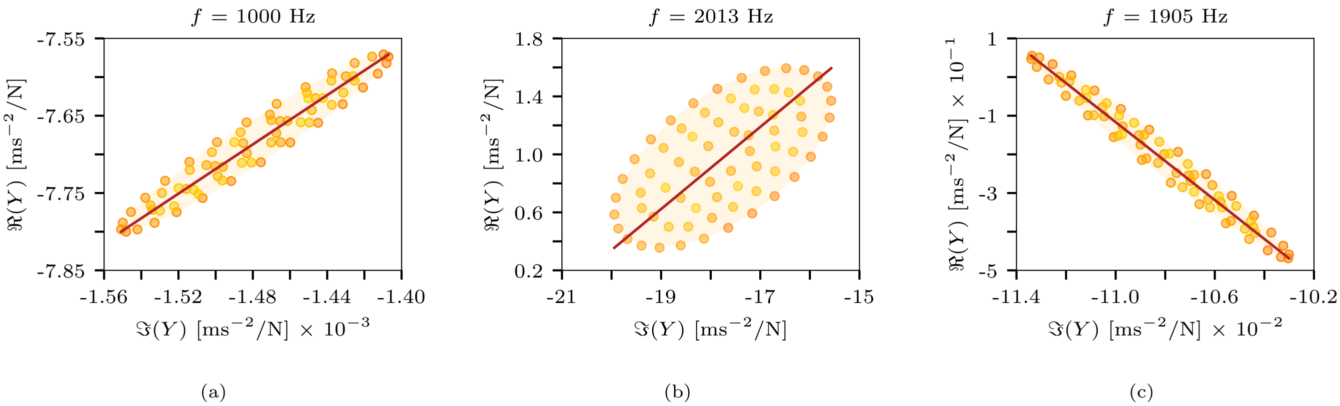

Figure 8: Elliptical shape of biased FRFs presented in complex plane for impact location A2 and sensor location 1, x-direction: a) at arbitrary frequency; b) at the resonance frequency; c) at the anti-resonance frequency.

imation approach. First, the relation of the real FRF part with respect to the bias is determined using the minimum and maximum values:

$$\Re(\mathbf{Y}) = k_{\mathrm{r}}\,\mathbf{b} + n_{\mathrm{r}}, \tag{12}$$

where:

$$k_{\mathrm{r}} = \frac{\max\big[\Re(\mathbf{Y})\big] - \min\big[\Re(\mathbf{Y})\big]}{2} \quad \text{and} \quad n_{\mathrm{r}} = \frac{\max\big[\Re(\mathbf{Y})\big] + \min\big[\Re(\mathbf{Y})\big]}{2}. \tag{13}$$

Matrix $\mathbf{Y}$ consists of the measured FRFs for several impact repetitions with bias errors and one response location. The bias values $\mathbf{b}$ are bounded between -1 and 1. Next, the relation between the real and imaginary parts for the ellipse's major axis is obtained, fitting data from the complex plane to the following equation:

$$\Im(\mathbf{Y}) = k_{\mathrm{i}}\,\Re(\mathbf{Y}) + n_{\mathrm{i}}. \tag{14}$$

Using Eqs. (12) and (14) the FRFs for multiple biases in the most sensitive direction can be reconstructed.

Step 3: Saltelli sampling scheme

The third step includes the generation of a large set of biased positions at each force input location. The Saltelli sample scheme[4] is used here to generate a bias distribution at the ellipse's major axis [18]. For each bias location, real and imaginary FRF parts are evaluated, and numerous FRFs are obtained (Fig. 9).

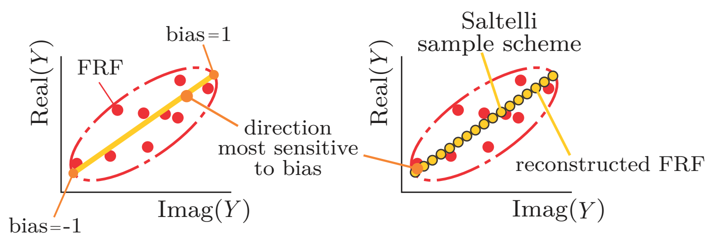

Figure 9: (Step 3.1) Reconstruction of multiple FRFs for each impact location using Saltelli sample scheme for set of biased excitation positions.

Note, that the coefficients k_r, k_i, n_r and n_i are frequency dependent, as depicted in Fig. 10. For each frequency, numerous biased FRFs are therefore reconstructed as:

$$\mathbf{Y}^{\mathrm{bias}} = \Re(\mathbf{Y}^{\mathrm{bias}}) + \mathrm{i}\,\Im(\mathbf{Y}^{\mathrm{bias}}). \tag{15}$$

It should be emphasized here that the direction most sensitive to bias is also dependent on the frequency. Therefore, biased FRFs, reconstructed on the basis of the approximation approach, are not consistent with the specific impact location across the entire frequency range. However, as the FBS is also frequency dependent, this is not to be considered problematic for future calculations using reconstructed FRFs regarding impact sensitivity indices, as at each frequency point the most influential impacts are included. An approximation approach also reduces the required computational power as only a single line of bias is considered instead of the entire area within an ellipse. The reconstructed FRFs are intended to be used for the sensitivity analysis only, i.e. to determine impact locations whose bias errors have greatest influence on the consistency of the

[4]The sample set is generated for number of input parameters equal to number of individual impact locations. Values of the sample set should be bounded by -1 and 1, which are the limits of bias values **b**.

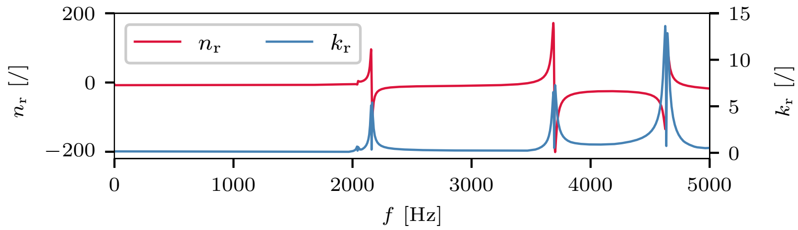

(a)

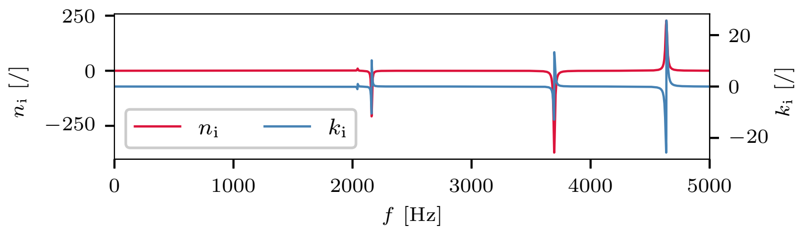

(b)

Figure 10: Coefficients for the reconstruction of the numerous biased FRFs; a) n_r and k_r, b) n_i and k_i.

VP. The use of reconstructed FRFs in the coupling process is discouraged and only the measured FRFs should be used. Due to the dependence of the FRFs' spread on the frequency reciprocity of the VP can also be evaluated for partial frequency bandwidths instead of averaging the criterium over the full range. In this manner, point-dependency of the anti-resonances can be controlled.

With the sizable FRF sample set available, each set of FRFs is then used in the VPT in order to obtain full-DoF FRFs at the VP. When performing the VPT on measured data, the value of impact offset is unknown and therefore the force transformation matrix $\mathbf{T}_\mathrm{f}$ is inconsistent. We propose to consciously use this inconsistency in the VPT and assemble $\mathbf{T}_\mathrm{f}$ using the desired (centered) impact position. The coherence criterion (Eq. 11) is then used to assess the overall reciprocity of the VP FRF matrix and with that the quality of the virtual point transformation. This is schematically shown in Fig. 11.

(Step 4) Global sensitivity analysis

In the fourth and final step of the methodology, a Sobol sensitivity analysis

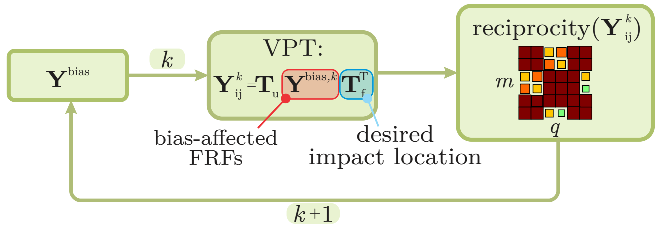

Figure 11: (Step 3.2) Estimation of VPT quality through the reciprocity criterion for all sets of biased FRFs.

is implemented on the set of reciprocity values from all the VP transformations[5]. With this approach, the bias on the impact locations that contribute significantly to the quality and repeatability of the VPT is recognized (Fig. 12).

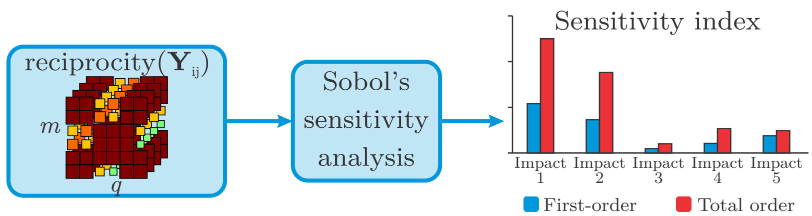

Figure 12: Step 4: Implementation of the Sobol sensitivity analysis to recognize biased impacts that strongly affect VP FRFs.

In this numerical case study the sensitivity analysis is carried out with two sets of input data considering the different magnitudes of the location offsets (Fig. 13). The first set considers the location offsets to be the same for all impact locations, and the second set suggests different magnitudes of the location offsets, as this is the more likely scenario in a real experiment.

Figure 14 shows the first-order Sobol's sensitivity indices for the whole VP reciprocity matrix for the location offset at points A15 and A6. Point A6 exhibits significantly higher values for all the off-diagonal DoFs in the reciprocity matrix.

[5]For more information on the Sobol sensitivity analysis and it's application to the bias characterization, the reader is referred to Appendix A

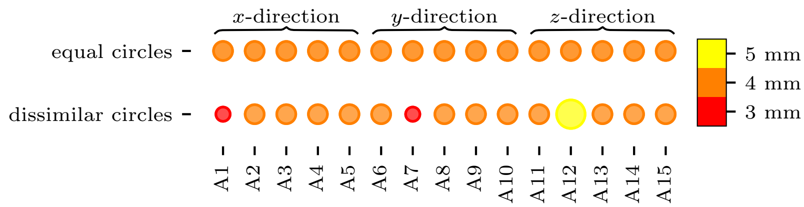

Figure 13: Magnitude of offset impacts for two different example sets.

It is, therefore, justifiable to take the mean value of the Sobol sensitivity index as a measure of the location offset's influence on the consistency of the VP. The nature of the reciprocity criterion must also be taken into account as the diagonal of the reciprocity matrix equals 1, by definition. Calculating the variance of the diagonal elements from the reciprocity matrix with respect to the bias is meaningless, as it stands $\mathbb{V}(\chi_{ii}) = 0$. Therefore, these should be omitted from the averaged sensitivity indices and are presented as hatched in Fig. 14.

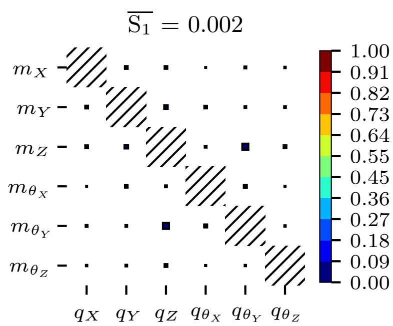

(a)

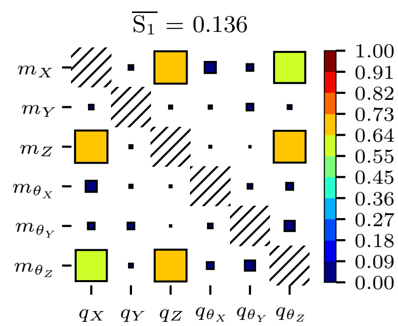

(b)

Figure 14: First-order Sobol sensitivity indices based on the reciprocity for all the VP DoFs for location offset in point; a) A15, b) A6.

The averaged indices for the individual impact location are shown in Fig. 15. Based on the first and the total order indices it is evident that the deviation in the location offset differs between the impact locations. It is interesting to note that the magnitude of the location offset (the difference between the set of equal and the set of dissimilar circles) has little influence on the results

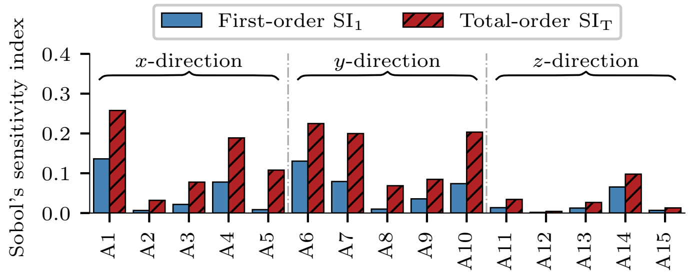

(a)

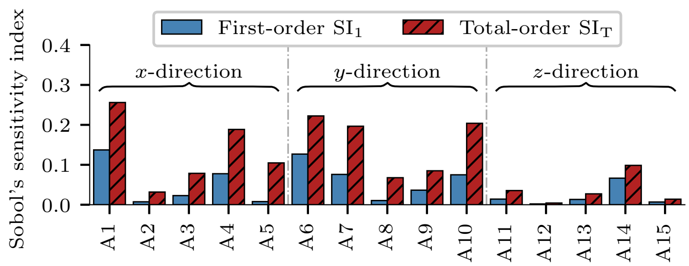

(b)

Figure 15: First and total order Sobol's sensitivity indices of reciprocity for two sets of impact offset magnitudes; a) equal circles, b) dissimilar circles

of the sensitivity analysis. Only slightly different values of the first and total order index can be observed for the impact locations A1, A7 and A12, where a different magnitude of the location offset is considered (set 2). Hence, it can be concluded that the selected impact location in correlation with the impact offset appears to be more influential than just the location offset itself.

As the entire methodology is presented on the numerical case study, the data for the perfectly centered impacts are also available. Therefore, the Sobol sensitivity analysis can be additionally carried out based on the coherence criterion (Eq. (11)), evaluated using the FRFs of the VP based on the biased impacts and the VP based on the centered impacts. The results of the sensitivity analysis for the equal circles only are presented in Fig. 16. It is advisable to compare Fig. 16 with Fig. 15a using only the first-order Sobol's sensitivity index as it measures the main effect of the individual impact alone. Using both approaches, the same

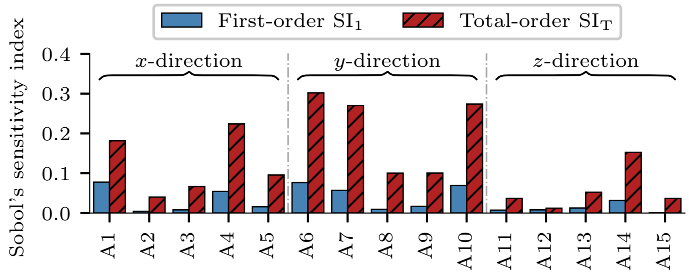

Figure 16: First and total order Sobol's sensitivity indices for equal impact offset magnitudes, using coherence criterion on VP FRFs, assembled using biased and centred impacts, respectively.

impacts can be recognized as bias-affected and therefore the use of reciprocity as the input for the sensitivity analysis is justified. This is especially convenient when performing experimental measurements as the reciprocity of the VP can always be accessed, although perfectly centered impacts are not available.

3.1 Sensitivity-based analysis of the VP consistency and the affect on coupling results

Based on the performed sensitivity analysis, it would make sense to only include the points in the virtual point transformation for which the deviation of the location offset has the smallest influence on the mean reciprocity of the VP transformation. In the example presented here, one impact location is excluded for every direction with the highest overall sensitivity index. The FRFs for impact locations at the points A1, A6 and A14 were omitted from the VP transformation. This set of impact locations is considered to have low (first-order) sensitivity to the location offset and is referred to as LOW SENS (Table 2). In order to demonstrate the importance of the correct selection of the impact locations, the so-called HIGH SENS impacts are also proposed, which contain impact location points that exhibit high (first-order) sensitivity to the location offset.

In order to objectively quantify the importance of the proper selection of the impact location with low sensitivity to position the offset, the consistency of the

Table 2: Impacts with low and high sensitivity to bias.

Impact location set	Impact locations											
LOW SENS	A2	A3	A4	A5	A7	A8	A9	A10	A11	A12	A13	A15
HIGH SENS	A1	A3	A4	A5	A6	A7	A9	A10	A11	A12	A13	A14
	x–direction				y–direction				z–direction			

coupling result is evaluated. The final assembly is shown in Fig. 17, along with the positions of the reference sensors and impact locations.

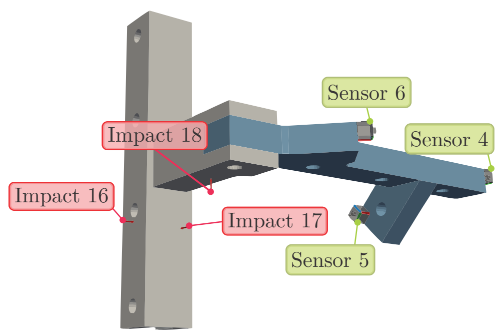

Figure 17: Structure AB with impact and sensor positions used for validation of the coupling results.

At each impact location, five biased impacts are randomly selected from the FRF set generated from the FEM model. In order to replicate the conditions imposed by the experiment, the selected FRFs are then averaged to minimize the effects of random errors introduced by the measurement conditions. By using the selection presented in Table 2 the VP FRFs (Figs. 18-19) are constructed using the LOW SENS and HIGH SENS impact sets separately. Additionally, all 15 biased impacts are also used to obtain the VP FRFs. Individual FRFs are evaluated relative to the reference VP, composed of a highly over-determined set of impacts and channels with no bias error. From Figs. 18-19 it is evident that by using the LOW SENS impact location set it is possible to increase the consistency of the VP transformation when compared to the reference. It can be

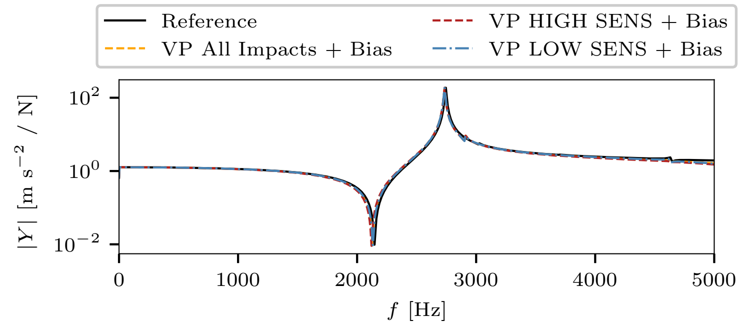

(a)

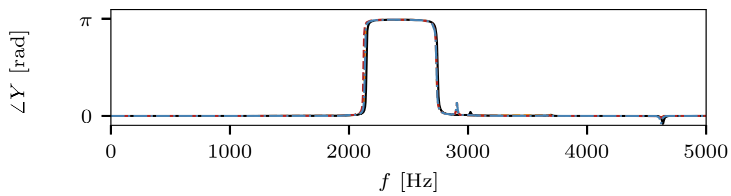

(b)

Figure 18: Comparison between B's VP FRFs for excitation in y-direction and response in y-direction using different sets of impacts; a) Magnitude, b) Phase.

seen that in the case of translational FRFs (Fig. 18), a relatively small difference between all the transformations can be observed. This is mainly due to the nature of the VP transformation, for which the translational FRFs are projected directly to the VP [20]. However, the biggest difference can be observed in the case of the rotational VP FRFs (Fig. 19), which are more subjected to the biased impact locations as the RDoFs are reconstructed based on the relative position of the impacts and responses to the VP. Here, it is clear that the FRF obtained with the LOW SENS impact locations set is in better agreement with the reference FRF across the whole frequency range. In particular, the positions of the anti-resonance regions are well aligned with the reference FRF.

In Fig. 20a the final coupling result for structures A and B is shown. In the case of structure A the VP is constructed by considering the impact locations with zero location offset, as stated previously. The coupling is performed using

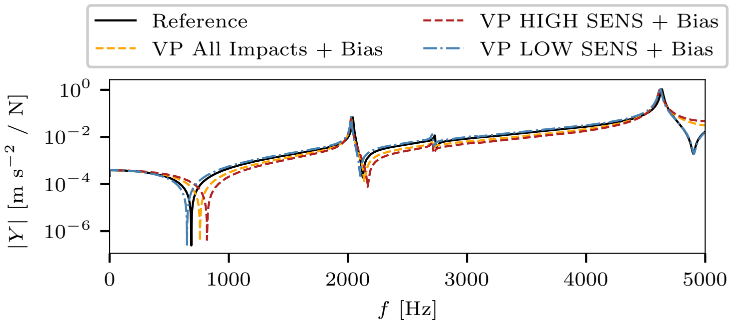

(a)

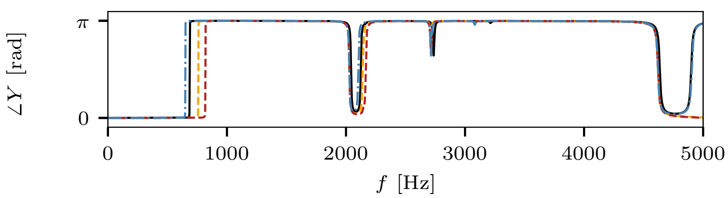

(b)

Figure 19: Comparison between B's VP FRFs for excitation in θ_y-direction and response in θ_y-direction using different sets of impacts; a) Magnitude, b) Phase.

the admittance $\mathbf{Y}^{\mathrm{B}}_{22}$ assembled from LOW SENS, HIGH SENS and also all 15 biased impact locations respectively. Additionally, the reference coupling result is set by using the VP with no bias errors. Based on a visual inspection, it can be concluded that the coupled FRF based on LOW SENS impacts matches the reference with better agreement. As for the coupling result based on all 15 and the HIGH SENS bias impacts, both FRFs are closely aligned; however, both differ significantly from the reference.

The phase of the coupled responses for different sets of impacts is investigated in Fig. 20b. Again we observe better agreement for the reference with the FRF based on LOW SENS impacts than with all or the HIGH SENS impacts.

The frequency-dependent coherence criterion for the coupled results S4$-x$/I17 is shown in Fig. 21. The coherence values for all the impact sets are obtained by calculating the coherence criterion against the reference FRFs. If the LOW

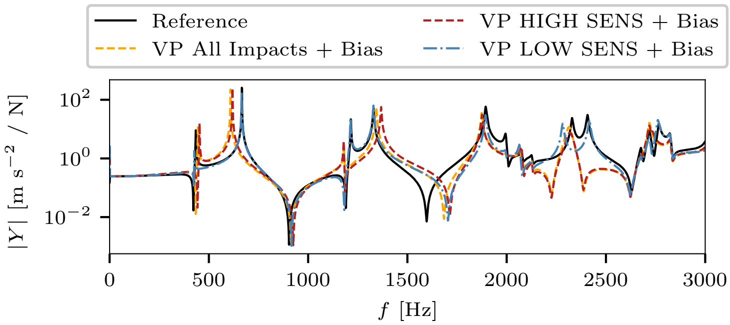

(a)

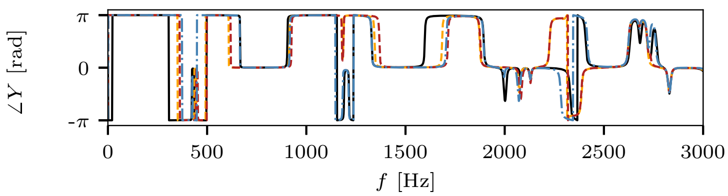

(b)

Figure 20: Comparison between final assembly FRFs S4$-x$/I17 using different sets of impacts in process of obtaining $\mathbf{Y}_{22}^{\mathrm{B}}$; a) Magnitude, b) Phase.

SENS impact location set is considered in the VP construction, a fairly good match with the reference FRFs can be identified in the coupling result. If the HIGH SENS set is considered in the coupling process, significant deviations from the reference measurements can be observed. The misalignment in terms of the amplitude and the position of the natural frequencies can be identified. Although we increased the number of excitations used in the VPT to 15 bias-affected impacts, this contributes little to the accuracy of the coupled response.

The frequency-averaged value of the coherence criterion is shown in Fig. 22. It is clear that the use of impacts that exhibit low sensitivity to the bias increases the overall consistency of the coupling procedure. Increased performance is observed when using the LOW SENS impacts, even when compared to the VPT based on all 15 biased impacts, indicating that the increase in the over-determination of the transformation does not entirely filter the bias errors from

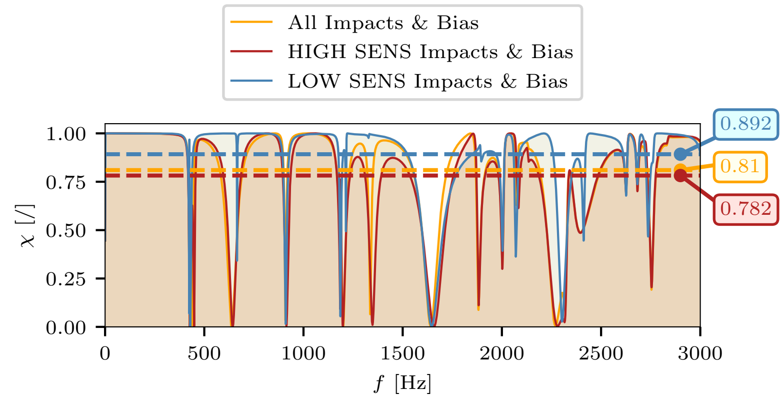

Figure 21: Frequency-dependent coherence criterion for final assembly response S4$-x$/I17 using different sets of impacts in the coupling process.

the VP FRFs.

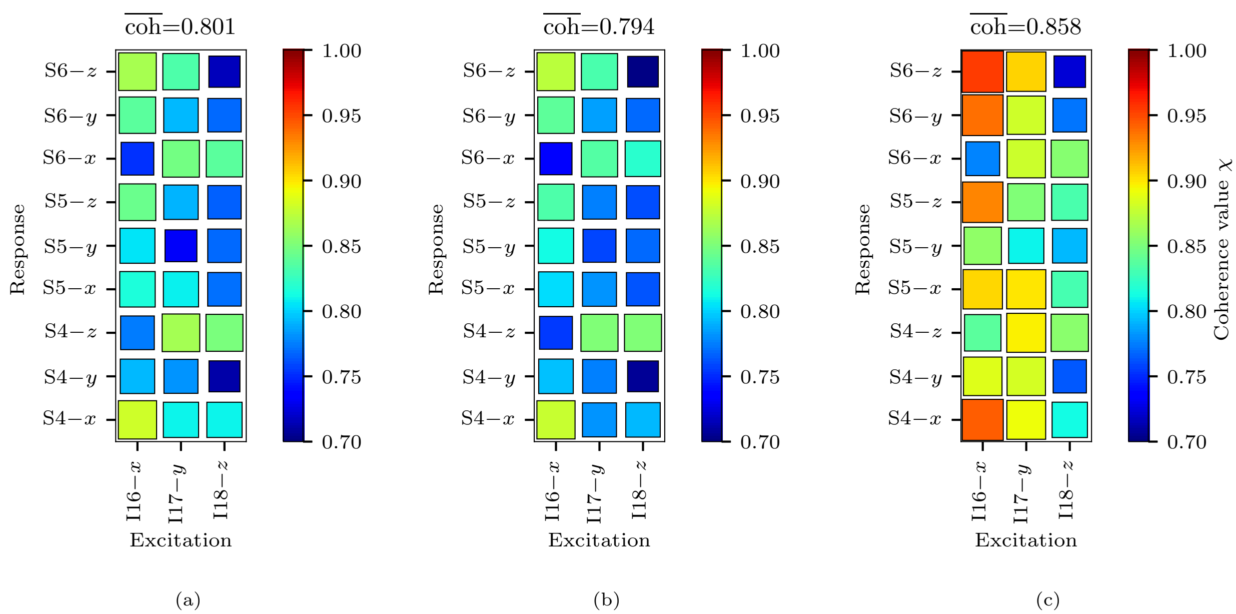

Figure 22: Frequency-averaged value of the coherence criterion between the investigated and reference FRFs. Investigated FRFs are assembled using $\mathbf{Y}_{22}^{\mathrm{B}}$ based on; a) All impacts, b) HIGH SENS Impacts, c) LOW SENS Impacts.

4 Experimental case study

This section demonstrates the practical applicability of the proposed sensitivity-based bias characterization method. The characterization is performed on a coupling application with the virtual point transformation. Similar to the numerical application, the VPT reciprocity is used as the quality indicator. Two beam-like structures (named A and B) are coupled together with a bolted connection. The assembled configuration is depicted in Fig. 23a. The structures were supported on polyurethane-foam blocks representing approximately free-free boundary conditions.

Six tri-axial accelerometers PCB 356A32 were used to measure the structure's response. Three of them were positioned around the interface at each substructure and three used as a reference. An automated impact hammer was utilized for the impact excitation (Fig. 23b) [21]. By using an automatic modal hammer, excellent repeatability between the impacts can be achieved. Moreover, the bias error in the excitation location can be minimized by careful positioning of the modal hammer.

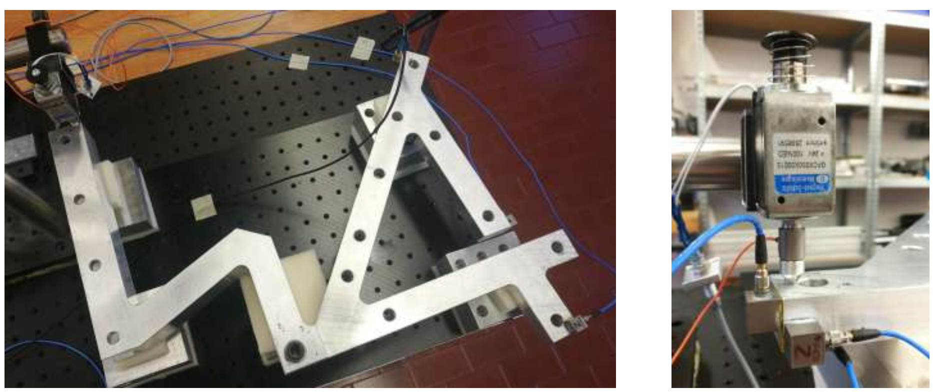

(a) (b)

Figure 23: Experimental setup; a) assembled configuration, b) interface of substructure A with automatic impact hammer.

Impacts around the interface for substructure A were obtained with precise positioning of the modal hammer. Therefore, bias errors in the excitation location can be neglected. For the impacts around the interface at substructure B, bias errors in the excitation location were introduced. The location of the impact was randomly varied within a 2 mm radius around the assumed impact location. This directly recreated real-life randomness that is commonly present with the impact excitation.

In Fig. 24 the measured FRFs from the distribution of the impact locations at substructure B are shown. The largest deviation can be observed in the location of the anti-resonance region. The small deviations in the measured FRFs are later used to reconstruct the FRFs based on the Saltelli sampling scheme, following the approach proposed in Section 3.

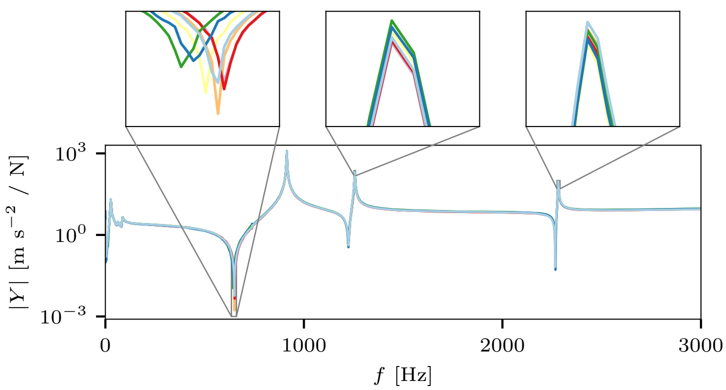

Figure 24: Bias-affected FRFs for impact location A11 and sensor location 1, x-direction.

The values of the reconstructed FRFs at a certain frequency location are depicted in Fig. 25. The linearity assumption for the reconstruction of the dominant directions is also valid on real experimental measurements.

After the reconstruction of the FRFs following Saltelli sample scheme a global sensitivity analysis can be performed. The virtual point reciprocity was used as a quality indicator. In Fig. 26a a high-sensitivity impact location on the whole virtual point reciprocity matrix is depicted. If we compare it with the low-sensitivity impact location in Fig. 26b, we can clearly select the most consistent set of impacts directly from the experimental measurements.

Again, averaging can be applied to determine the bias error influence from

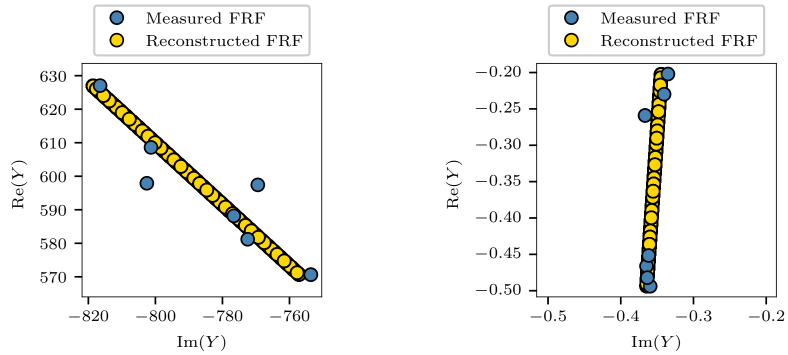

(a) (b)

Figure 25: Comparison of reconstructed and measured value of FRFs at a selected frequency: a) resonant frequency 914 Hz, b) anti-resonant frequency 1224 Hz.

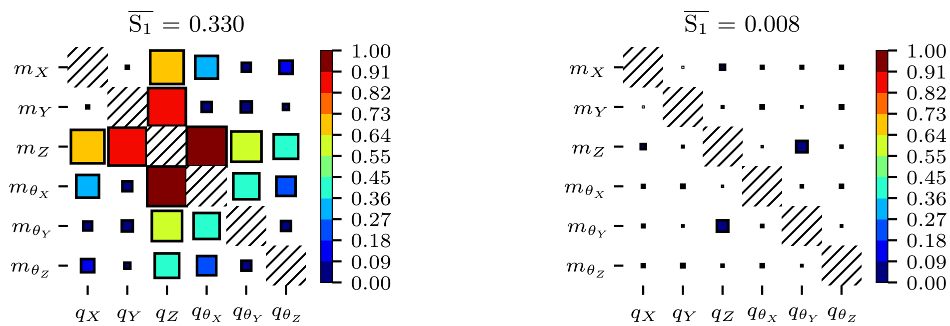

(a) (b)

Figure 26: First-order Sobol sensitivity indices based on reciprocity for all VP DoFs for a location offset in point; a) A14, b) A15.

entire reciprocity matrix. In Fig. 27 the averaged first- and total-order Sobol's sensitivity indices are depicted for all 15 impact locations around the interface. Three impact locations are shown to have a high sensitivity to bias (A1, A10, A14); therefore, they should be removed from the transformation and the final coupling results. With the listed impacts omitted, the LOW SENS impact set is assembled to be applied to the VPT, along with the impact set where all the impacts are retained.

The final step was the application of a coupling procedure with different impact locations included in the virtual point transformation. A comparison

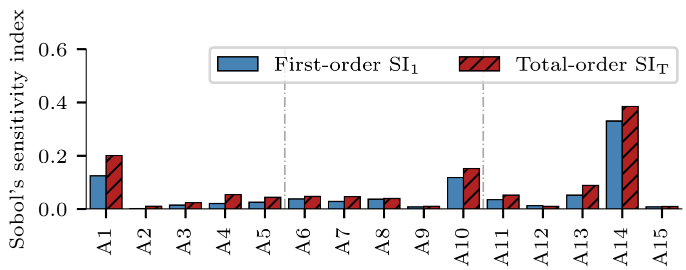

Figure 27: Averaged First- and Total-order Sobol's sensitivity indices for all 15 impact locations.

of the VP FRFs is presented first (Fig. 28), with all the impacts, with a LOW SENS set and a reference set of impacts[6]. By removing the identified bad impact locations from the transformation, better results can be obtained. The best improvement can be observed around 2.5 kHz, where the prediction with all the impact locations erroneously predicts the anti-resonance region.

The coupling FRFs are obtained with Eq. (5). Reference impacts and channels used for the validation of the coupling results are depicted in Fig. 29. In Fig. 30, the FRF S4-z/I17 is shown based on all sets and the LOW SENS sets of impacts. Only minor differences can be observed in the amplitude and phase prediction; however, Y_{31}^{AB} based on LOW SENS impacts matches with the reference with the higher degree of accuracy compared to the VP with all the impacts. An improved prediction of the FRF by excluding the impacts with a high sensitivity index is apparent in the high frequency-range.

The overall agreement between the reference FRF and the predicted coupled FRFs based on all and the LOW SENS impacts is evaluated using the coherence criterion. The criterion is calculated for the entire analysed frequency range and then averaged (Fig. 31). The overall increase in the criterion values is observed when the impacts with a high sensitivity index are omitted from the coupling

[6]A reference set of impacts was placed directly on the intended excitation location; therefore, a close-to-zero bias error can be assumed at those locations.

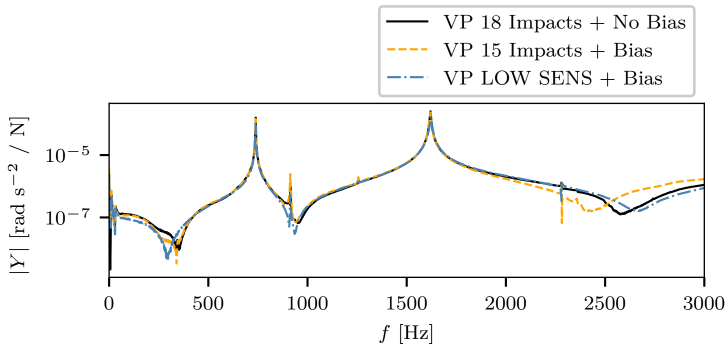

(a)

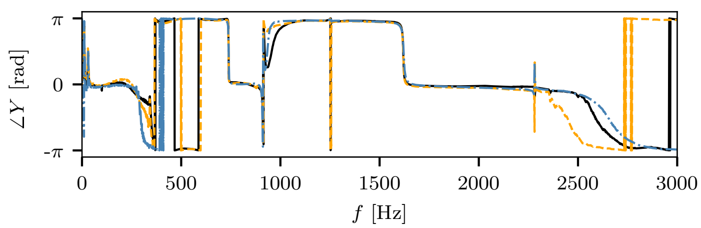

(b)

Figure 28: Comparison between B's VP FRFs for excitation in θ_y-direction and response in θ_y-direction using different sets of impacts; a) Magnitude, b) Phase.

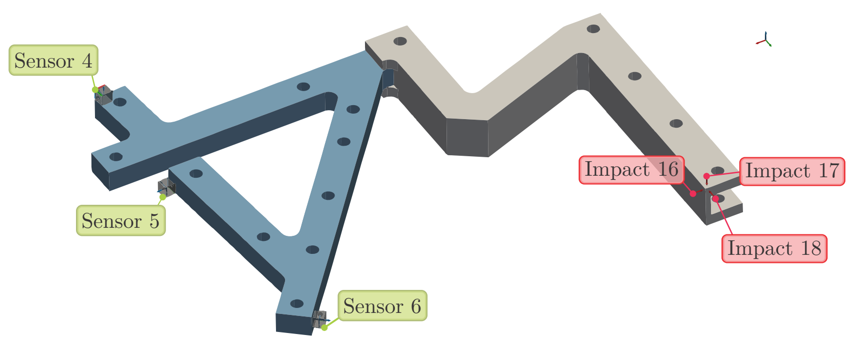

Figure 29: Experimental setup on AB with impact and sensor positions used for validation of the coupling results.

process.

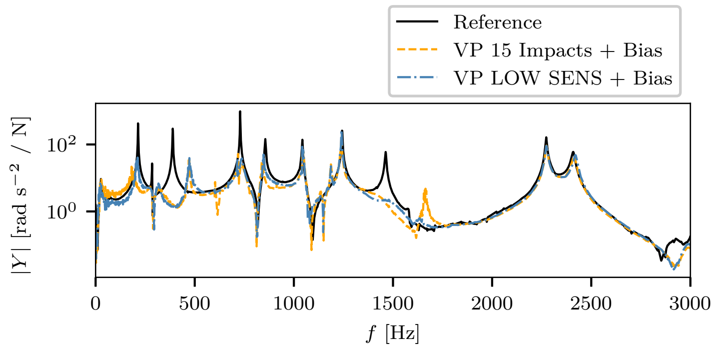

(a)

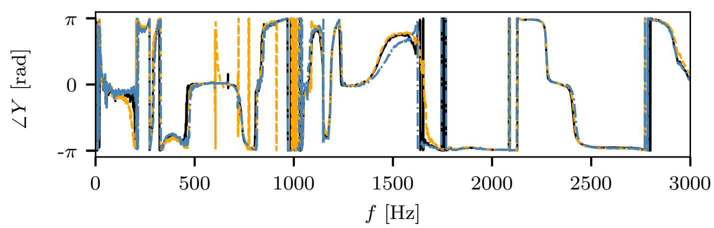

(b)

Figure 30: Comparison of the final assembly FRF S4-z/I17 obtained with all and LOW SENS sets of impacts, together with a reference measurement; a) Magnitude, b) Phase.

4.1 Discussion

The sensitivity-based approach to bias characterization can be used to identify possible sources of systematic error directly on the experimental model. This can be very beneficial since one does not need to redo all the measurements to perform the identification. The identification can be performed with both a coupling and a decoupling applications, since the only requirement is randomness on the input excitation and selection of the quality indicator on which the identification is performed. If we were to add bias to the location of the transducers, the approach could be utilized to identify the most sensitive output locations to bias. Therefore, it can be concluded that the sensitivity-based approach can identify the bias directly from experimental measurements.

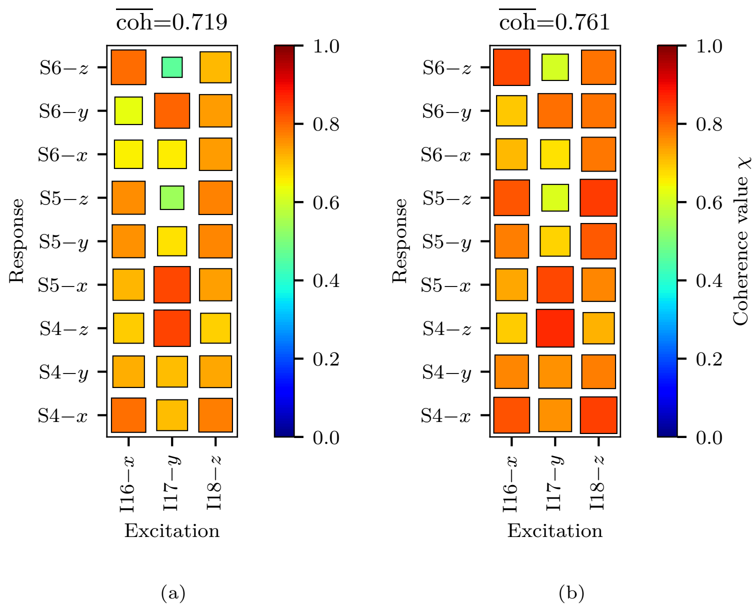

Figure 31: Frequency-averaged value of the coherence criterion between the investigated and reference FRFs. Investigated FRFs are assembled using $\mathbf{Y}_{22}^{\mathrm{B}}$ based on; a) All impacts, b) LOW SENS Impacts.

5 Conclusion

A reliable application of experimental frequency based substructuring on complex structures remains challenging due to the numerous possible sources of error. One of the primary sources with an impact excitation is the uncertainty in the location and orientation of the impact. A small deviation in the location of the impact affects the acquired FRF throughout the whole frequency range. This can directly yield erroneous coupling results.

In this work, an approach to characterize the bias at the impact location was proposed. The methodology makes it possible to estimate the bias error directly from experimental measurements without the need for an additional numerical model or dedicated experimental setup. The small random locations from the impact excitation by hand are used to reconstruct a range of FRFs based on the Saltelli sample scheme. Later, a Sobol global sensitivity analysis is used to characterize the effect of bias based on an arbitrary quality indicator. It was shown that the methodology successfully predicts the worst impact excitation locations based on the VP quality indicator. Furthermore, by discarding the worst locations in the transformation, more reliable coupling results could be obtained. The idea is applicable to all frequency based substructuring methodologies, as well as, transfer path analysis applications.

Acknowledgements

The authors acknowledge partial financial support from the core research funding P2-0263 and the applied research project L2-1837, both financed by ARRS, the Slovenian research agency.

Appendix A Sobol sensitivity analysis

In this appendix the key steps to calculate the sensitivity indexes with the Sobol sensitivity analysis [17, 18] are presented. The reason Sobol sensitivity analysis is proposed here is the computation algorithm that allows an estimation of the global sensitivity indexes using only the output values of the proposed evaluation model.

Adopting reciprocity criterion of the virtual point FRFs as an indicator of the VPT quality, the evaluation model can be established as follows (see Eq. (11) for more detail):

$$\chi_{ij}(b_1, \ldots, b_l, \ldots, b_n) = \mathrm{coh}\big(Y_{ij},\, Y_{ji}\big), \quad Y_{ij},\, Y_{ji} \in \mathbf{Y}_{\mathrm{qm}}. \tag{A.1}$$

Here b_l is the value of bias error at l-th impact location for total (n) impact locations. In other words, for each sample set from Saltelli sample scheme VPT is performed and reciprocity check is carried out to obtain 6×6 reciprocity matrix.

In the following, the first-order Sobol's sensitivity index is calculated for each input parameter b_l at each DoF:

$$S_1^{\chi_{ij}} = \frac{\mathbb{V}_{b_l}\big(\mathbb{E}_{b_{\sim l}}[\chi_{ij}|b_l]\big)}{\mathbb{V}(\chi_{ij})}, \tag{A.2}$$

where $\mathbb{V}$ is the variance operator, $\mathbb{E}$ the expectation operator and $b_{\sim l}$ the set of all input parameters apart from b_l. $\mathbb{E}_{b_{\sim l}}[\chi_{ij}|b_l]$ is the average of χ_{ij} over all possible values $b_{\sim l}$ while b_l is fixed. The outer variance is then taken over all possible values of b_l. First-order index measures the contribution of bias error at l-th excitation location alone to the total variance $\mathbb{V}\big(\chi_{ij}\big)$.

Similarly, total order index is evaluated that measures the effect of parameter b_l, including all higher-order interactions with other input parameters:

$$S_{\mathrm{T}}^{\chi_{ij}} = 1 - \frac{\mathbb{V}_{b_{\sim l}}\big(\mathbb{E}_{b_l}[\chi_{ij}|b_{\sim l}]\big)}{\mathbb{V}(\chi_{ij})}, \tag{A.3}$$

where $\mathbb{V}_{b_{\sim l}}\big(\mathbb{E}_{b_l}[\chi_{ij}|b_{\sim l}]\big)/\mathbb{V}(\chi_{ij})$ is the first-order effect of $b_{\sim l}$.

References

[1] M. van der Seijs, Experimental dynamic substructuring: Analysis and design strategies for vehicle development, Ph.D. thesis, Delft University of Technology (2016).

[2] B. Starc, G. Čepon, M. Boltežar, The influence of washing machine-leg hardness on its dynamics response within component-mode synthesis techniques, International Journal of Mechanical Sciences 127 (2017) 23–30.

[3] D. De Klerk, D. Rixen, S. Voormeeren, General framework for dynamic substructuring: history, review and classification of techniques, AIAA journal 46 (5) (2008) 1169–1181.

[4] A. Drozg, G. Čepon, M. Boltežar, Full-degrees-of-freedom frequency based substructuring, Mechanical Systems and Signal Processing 98 (2018) 570–579.

[5] D. Rixen, How measurement inaccuracies induce spurious peaks in frequency based substructuring, in: Proceedings of the Twenty Sixth International Modal Analysis Conference, Orlando, FL. Society for Experimental Mechanics, Bethel, CT, 2008.

[6] D. De Klerk, R. Visser, Characterization of measurement errors in experimental frequency based substructuring, ISMA 2010 Including USD2010 (2010) 1881–90.

[7] M. Kodrič, G. Čepon, M. Boltežar, Experimental framework for identifying inconsistent measurements in frequency-based substructuring, Mechanical Systems and Signal Processing 154 (2020) 107562.

[8] S. Voormeeren, D. Rixen, Substructure decoupling techniques–a review and uncertainty propagation analysis, in: Proceedings of the Twenty-Seventh International Modal Analysis Conference, Orlando, Florida, 2009.

[9] J. Meggitt, A. Moorhouse, A covariance based framework for the propagation of correlated uncertainty in frequency based dynamic sub-structuring, Mechanical Systems and Signal Processing 136 (2020) 106505.

[10] F. Trainotti, M. Haeussler, D. Rixen, A practical handling of measurement uncertainties in frequency based substructuring, Mechanical Systems and Signal Processing 144 (2020) 106846.

[11] D. De Klerk, D. Rixen, S. Voormeeren, F. Pasteuning, Solving the rdof problem in experimental dynamic substructuring, in: Proceedings of the Twentysixth International Modal Analysis Conference, Orlando, FL, 2008.

[12] M. van der Seijs, D. van den Bosch, D. Rixen, D. de Klerk, An improved methodology for the virtual point transformation of measured frequency response functions in dynamic substructuring, COMPDYN (2013).

[13] E. Pasma, M. van der Seijs, S. Klaassen, M. van der Kooij, Frequency based substructuring with the virtual point transformation, flexible interface modes and a transmission simulator, in: Dynamics of Coupled Structures, Volume 4, Springer, 2018, pp. 205–213.

[14] D. De Klerk, How bias errors affect experimental dynamic substructuring, in: Structural Dynamics, Volume 3, Springer, 2011, pp. 1101–1112.

[15] M. Haeussler, S. Sendlbeck, D. Rixen, Automated correction of sensor orientation in experimental dynamic substructuring, in: Dynamics of Coupled Structures, Volume 4, Springer, 2018, pp. 65–70.

[16] A. Saltelli, Making best use of model evaluations to compute sensitivity indices, Computer physics communications 145 (2) (2002) 280–297.

[17] I. M. Sobol, Global sensitivity indices for nonlinear mathematical models and their monte carlo estimates, Mathematics and computers in simulation 55 (1-3) (2001) 271–280.

[18] A. Saltelli, P. Annoni, I. Azzini, F. Campolongo, M. Ratto, S. Tarantola, Variance based sensitivity analysis of model output. Design and estimator for the total sensitivity index, Computer physics communications 181 (2) (2010) 259–270.

[19] T. Bregar, A. El Mahmoudi, M. Kodrič, G. Čepon, M. Boltežar, D. J. Rixen, Introducing pyFBS: An open-source python package for frequency based substructuring and transfer path analysis, in: IMAC, 2021.

[20] T. Bregar, N. Holeček, G. Čepon, D. Rixen, M. Boltežar, Including directly measured rotations in the virtual point transformation, Mechanical Systems and Signal Processing 141 (2020) 106440.

[21] J. Maierhofer, A. El Mahmoudi, D. Rixen, Development of a low cost automatic modal hammer for applications in substructuring, in: Dynamic Substructures, Volume 4, Springer, 2020, pp. 77–86.